[Geophysical Research Letters]

Supporting Information for

Climate impacts in delayed mitigation and geoengineering scenarios

S. Tilmes[1], B. M. Sanderson[1], and B. O'Neill[1]

[1]National Center for Atmospheric Research, Boulder CO, 80301

Contents of this file

Scenario Development using the ISAM model

The Late Decarbonization (LD) pathway is an emissions pathway, which represents no near-term mitigation activity until 2040. After 2040, the emissions reduction represents the maximum rate of decarbonization seen in the literature. All emissions follow RCP8.5 exactly until 2040, based on total CO_2 emissions (fossil fuel, cement, land use). After 2040, emissions transition to a period of peak decarbonization. The maximum rate of decarbonization is informed using the peak rate of decarbonization present in the Shared Socioeconomic Pathway (SSP) database (as accessed in December 2015, where the peak rate of annual CO_2 emissions reduction was -1318 $MtCO_2$/yr/yr in SSP5/RCP3.4 between 2060 and 2080). The maximum annual negative emissions rate is informed also using 2100 net negative emissions for SSP5/RCP2.6 (-18.3$GtCO_2$/yr - as accessed in December 2015). These constraints are implemented using a simple functional form for total CO_2 emissions

such that:

$$E_{CO2}^{overshoot}(t) = E_{CO2}^{RCP8.5} \qquad t < 2040$$
$$E_{CO2}^{overshoot}(t) = A(t - t_e)e^{-t/\tau} - E_\infty \qquad t \geq 2040$$

leaving 4 free parameters: A , t_e , τ , and E_∞ , for which we solve with the following boundary conditions:

$$E_{CO2}^{overshoot}(2040) = E_{RCP8.5}(2040)$$
$$dE_{CO2}^{overshoot}/dt(2040) = dE_{CO2}^{RCP8.5}/dt(2040)$$
$$E_{CO2}^{overshoot}(t \to \infty) = -18.3\text{GtCO2/yr}$$
$$\min\left(dE_{CO2}^{overshoot}/dt(t)\right) = -1.3\ \text{GtCO2/yr/yr}$$

such that the rate of change of emissions in 2040 is continuous with RCP8.5, but then emissions decline to a peak rate of decarbonization and then asymptote to a long term CO_2 removal level. CO_2 emissions thus peak in emissions in 2050 and then decline. Non-CO_2 emissions are computed from the CO_2 pathway as follows:

$$E_i^{overshoot}(t) = \max\left(E_{RCP8.5}^i(2040)\frac{E_{RCP8.5}^{CO2}(t)}{E_{RCP8.5}^{CO2}(2040)}, E_{RCP2.6}^i(t)\right)$$

Hence, emissions (E) of a given type *i* for a given year *t* are scaled such that the relative emission rates to RCP8.5 2040 values are kept constant with the CO_2 pathway, until emissions rates are less than those seen in RCP2.6 (in this case, the RCP2.6 values are used (see Figures S1b-d).

These emissions pathways are then used with the ISAM simple climate model, which is tuned to emulate the global mean climate response of CESM1-CAM5. The results of the simple climate simulations are shown in Figure S2. In addition to simulating the LD pathway, we also compute two geoengineering pathways using the ISAM model. In each case, the greenhouse gas emissions are identical to the LD scenario, but the sulfur emissions

are iteratively adjusted such that global mean temperatures remain steady at a given threshold (either 2 or 2.5 degrees C above preindustrial values), until no more sulfur injection is necessary to remain at the threshold. After this date, sulfur emissions remain at zero and the global mean temperature continues to decrease as carbon is removed from the atmosphere. The resulting difference in shortwave top of atmosphere flux from the LDP simulations and the overshoot simulations then informs the required forcing required for the CESM experiments (see Figure S2a).

Surface Energy Budget

Global precipitation trends for the different pathways differ largely in the last half of the 21st century. The reason for differences can be explained by changes in the surface energy budget. We analyze changes in the global surface energy budget between 2070-2099 and 2040-2055 and between 2170-2199 and 2040-2055 (Figure S5). A detailed summary of the shortwave (SW) energy budget is shown in Figure S5 (top panel); the total (SW+longwave) energy budget is shown in Figure S5 (bottom panel).

Incoming SW radiation is to the most part absorbed at the Earth's surface [*Trenberth et al.*, 2009]. Some of the energy is absorbed in the atmosphere while a fraction is also reflected by clouds, aerosols and the surface. The absorbed energy radiates back as longwave (LW) radiation. With the presence of greenhouse gases, this results in a warming of the troposphere. Some SW energy is transformed into latent heat and to a much smaller part into sensible heat.

The balance between incoming and outgoing net radiation keeps the climate in a steady state. However, changes in greenhouse gas and other forcings, like aerosols, change the atmospheric energy balance and result in changes in latent and sensible heat fluxes, and therefore surface temperature and precipitation.

The SW downwelling clear sky component (Figure S5, red bar) is reduced for scenarios with increasing greenhouse gases until 2070-99, as is the case for RCP8.5 and the LD pathway. Increasing temperatures in the tropopause enhance the abundance of water vapor and methane in the stratosphere, reflecting more SW radiation back to space. This effect overwhelms the increase in cloudy-sky SW radiation at the surface that is the result of the reduction in the tropospheric aerosol burden between 2040 and 2080 (*Boucher et al*., 2013). In SSI-2.0 and SSI-2.5, the SW downwelling component is reduced due to the dimming of the SW radiation from the artificially increased aerosol burden in the stratosphere, with the strongest reduction in SSI-2.0. In contrast, in the ED pathway, the dominant factor that increases the SW downwelling clear sky component is reduction in tropospheric aerosols. Reductions due to changes in greenhouse gases are not expected since temperatures are stabilized after 2040 in EDP (The same is the case for 2170-2199 for all scenarios).

The SW downwelling cloudy sky component is increased (green) in all pathways in 2070-99 compared to 2040-55. The reduction of tropospheric aerosols between 2040 and 2080 also impact the indirect effect of clouds. This effect should be slightly stronger in the ED pathway than in the other pathways, since it is based on different aerosol emission. In addition to the indirect effect, SSI-2.5 and SSI-2.0 show an even stronger increase in the SW downwelling cloudy sky component. The reducing of SW downwelling clear sky component reduces the latent heat flux at the surface (discussed below), and therefore reduces the formation of clouds (e.g., *Schmidt et al*, 2012).

The SW upwelling component (blue) illustrates the reflection of SW radiation from the surface back to space. This component is controlled by the amount of incoming SW radiation, but also largely controlled by changes in the sea-ice area. Since all components in Figure S5 are positive downward, the increase in this component equals the reduced

reflection back to space. The strongest occurs in RCP8.5, where surface warming causes the largest reduction in sea-ice, while this component is close to zero for the ED pathway, where sea-ice is stabilized. The artificial reduction in SW radiation in SSI also reduces the SW upwelling component.

The discussed changes result in an increase of net SW radiation change (top panel black crosses) between 2070-99 and 2040-2055 for EDP. For RCP8.5 and the LDP, net changes in the SW are almost balanced. With increasing solar dimming in SSI, net SW radiation change becomes more negative. For 2170-2199, changes in tropospheric aerosols are the main driver for the increase in SW radiation reaching the surface compared to 2040-2055, as SSI is no longer applied to the system.

What is more relevant to the hydrological cycle is the total surface energy budget, shown in Figure S5, bottom panel, including changes in net SW (red), net longwave (LW) (green), and net turbulent fluxes (blue), which include sensible and latent heat fluxes. The increase in greenhouse gases in the atmosphere, for RCP8.5 and LD scenarios, results in increasing net LW radiation, due to the stronger LW absorption of energy in the troposphere. Reductions in the net turbulent fluxes (downward positive), align with an increase in latent and sensible heat flux into the atmosphere, and therefore an increase in evaporation and heating. This causes a speed up of the hydrological cycle.

For the ED pathway, increases in the SW radiation is balanced by reductions in the LW heating and downward turbulent fluxes, resulting in a net negative downward energy flux. The increase in SW radiation due to the reduction of tropospheric aerosols results in an increase in latent and sensible heat flux into the atmosphere and also in an increase in precipitation.

With reductions in the SW radiation in SSI-2.0, the speed up of the hydrological cycles in a warming climate is reversed by 2070-2099. Opposing the other pathways, this results to

an increase in turbulent fluxes and therefore a slow-down of the hydrological cycles, as discussed in earlier studies (e.g., *Tilmes et al*., 2013). By the end of the 22nd century, this trend has been reversed for SSI-2.0 because geoengineering is no longer being applied; and as in the other cases, downward turbulent fluxes are negative (i.e. increased precipitation as in Figure S4), which is more similar to the ED pathway in 2070-2099 period.

Reference:

Trenberth, K. E., J. T. Fasullo, and J, Kiehl (2009) Earth's global energy budget. *Bulletin of the American Meteorological Society* 90.3, 311-323.

Boucher, O., D. Randall, P. Artaxo, C. Bretherton, G. Feingold, P. Forster, V.-M. Kerminen, Y. Kondo, H. Liao, U. Lohmann, P. Rasch, S. K. Satheesh, S. Sherwood, B. Stevens and X. Y. Zhang (2013). Clouds and Aerosols. In: Climate Change 2013: The Physical Science Basis. Contribution of Working Group I to the Fifth Assessment Report of the Intergovernmental Panel on Climate Change [Stocker, T.F., D. Qin, G.-K. Plattner, M. Tignor, S.K. Allen, J. Boschung, A. Nauels, Y. Xia, V. Bex and P.M. Midgley (eds.)]." Cambridge University Press, Cambridge, United Kingdom and New York, NY, USA

Tilmes, S., J. Fasullo, J.-F. Lamarque, D. R. Marsh, M. Mills, K. Alterskjaer, H. Muri, J. E. Kristja´nsson, O. Boucher, M. Schulz, J. N. S. Cole, C. L. Curry, A. Jones, J. Hay- wood, P. J. Irvine, D. Ji, J. C. Moore, D. B. Karam, B. Kravitz, P. J. Rasch, B. Singh, J.-H. Yoon, U. Niemeier, H. Schmidt, A. Robock, S. Yang, and S. Watanabe

(2013), The hydrological impact of geoengineering in the Geoengineering Model Intercom- parison Project (GeoMIP), *Journal of Geophysical Research: Atmospheres*, *118*(19), 11,036–11,058, doi:10.1002/jgrd.50868.

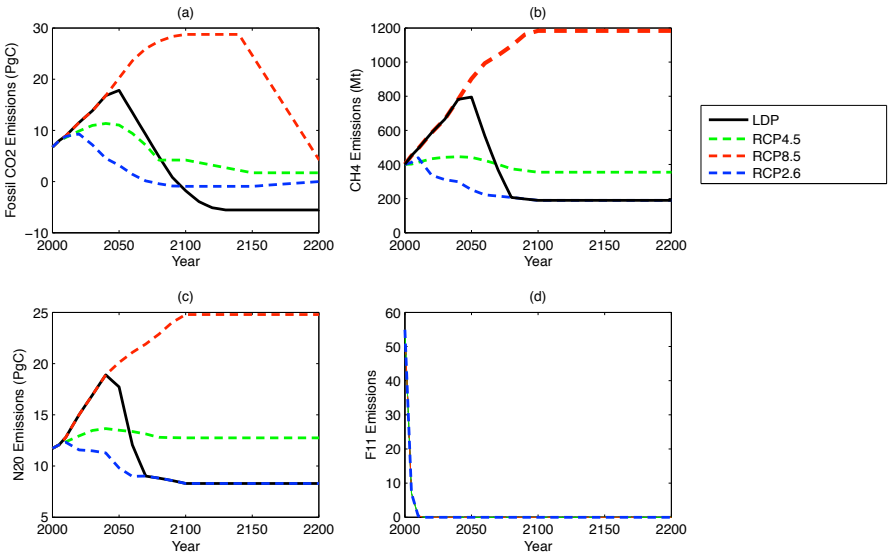

Figure S1: ISAM derived CO_2 (a), methane (b), nitrous oxide (c), and chlorofluorocarbons (d) emission evolution for the LD pathway (black) and other RCP pathways.

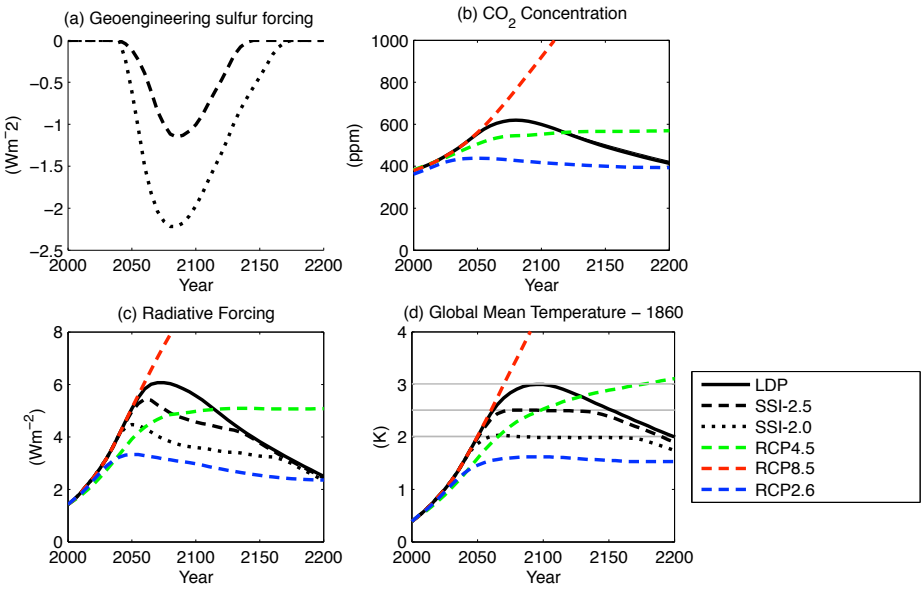

Figure S2: ISAM derived required time varying geoengineering sulfur forcing required for SSI-2.5 (dashed) and SSI-2.0 (dotted) (a), CO_2 concentrations (b), the resulting radiative forcing for different pathways (c), and global mean temperature with regard to pre-industrial conditions (d).

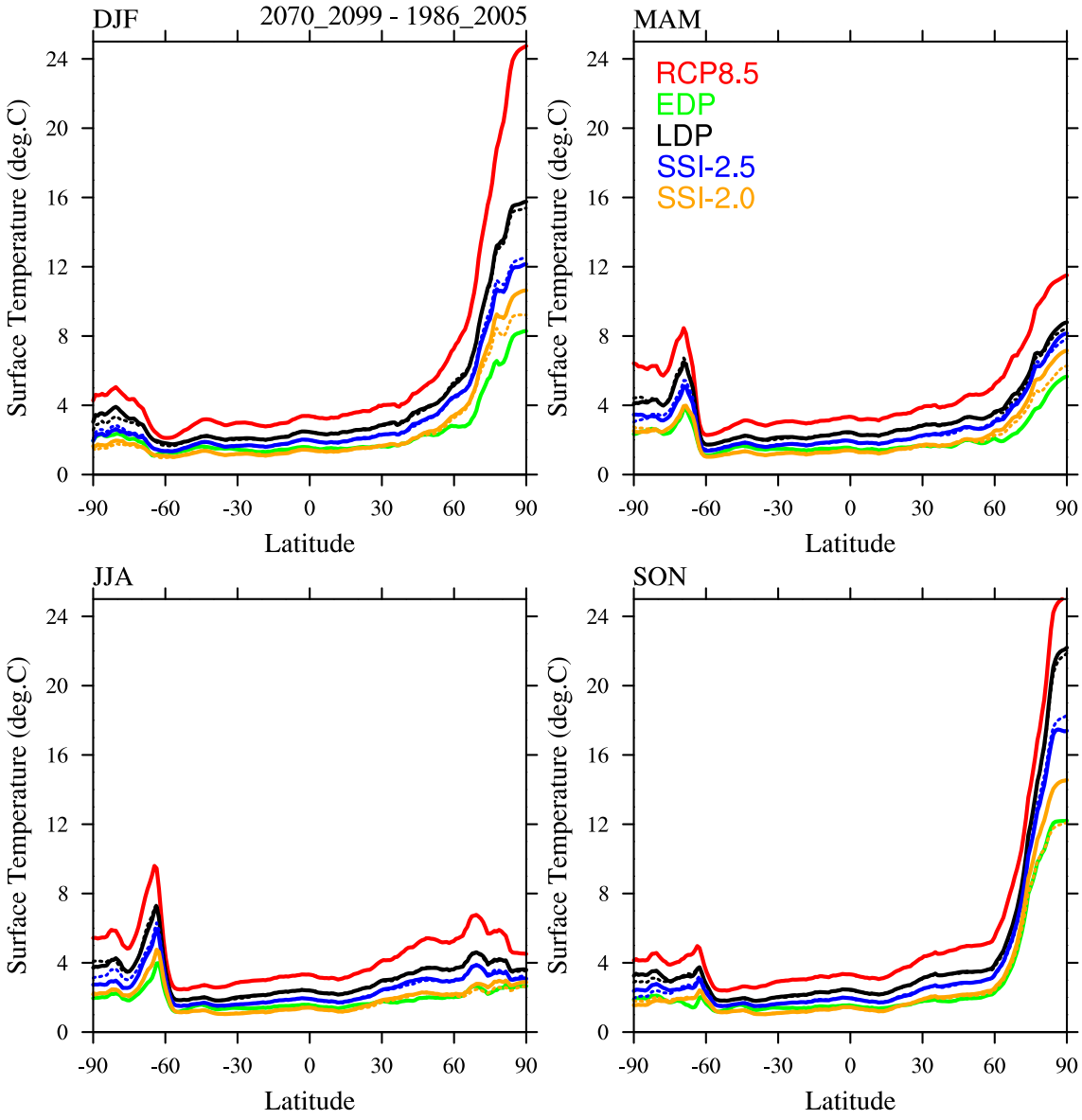

Figure S3: Zonal average temperature change between 2070-2099 and 1986-2005 for different pathways and different seasons: December-January-February (top left), March-April-May (top right), June-July-August (bottom left), September-October-November (bottom right).

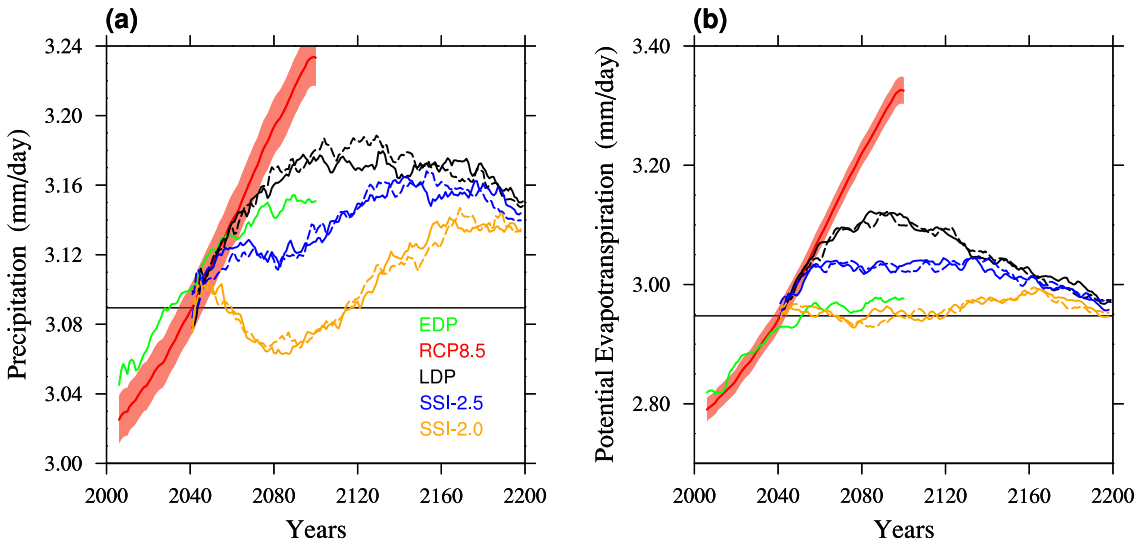

Figure S4: Time evolution of global and annual average global precipitation (a) and Potential Evapotranspiration (PET)) (b), for different scenarios. A ten year running mean was applied. Different colors identify different experiments (see legend). For RCP8.5, shaded areas indicate the standard deviation of results including all 30 members of the large ensemble.

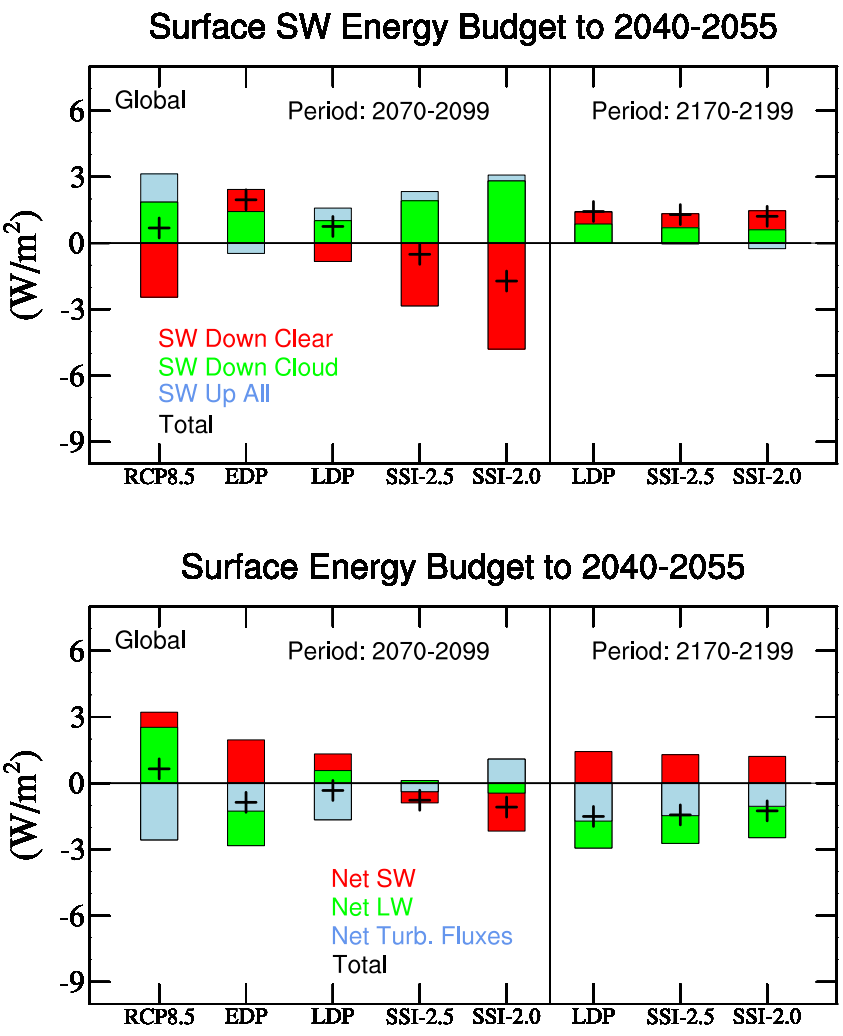

Figure S5: Top Panel: Annual change of shortwave (SW) surface energy fluxes for different experiments and periods, 2070-2099 (left) and 2170-2199 (right) in comparison to 2040-2050: SW downwelling clear sky (red), SW downwelling cloudy sky (green), SW upwelling (blue), and total fluxes (SW clear sky+SW downwelling_ cloudy sky + SW upwelling, black plus signs). All flux terms are positive downward. Bottom panel: Surface energy budget for different experiments and periods, 2070-2099 (left) and 2170-2199 (right) in comparison to 2040-2050: Net SW (red), net long wave (LW) (green), net turbulent (blue), total fluxes (black plus signs). All flux terms are positive downward.

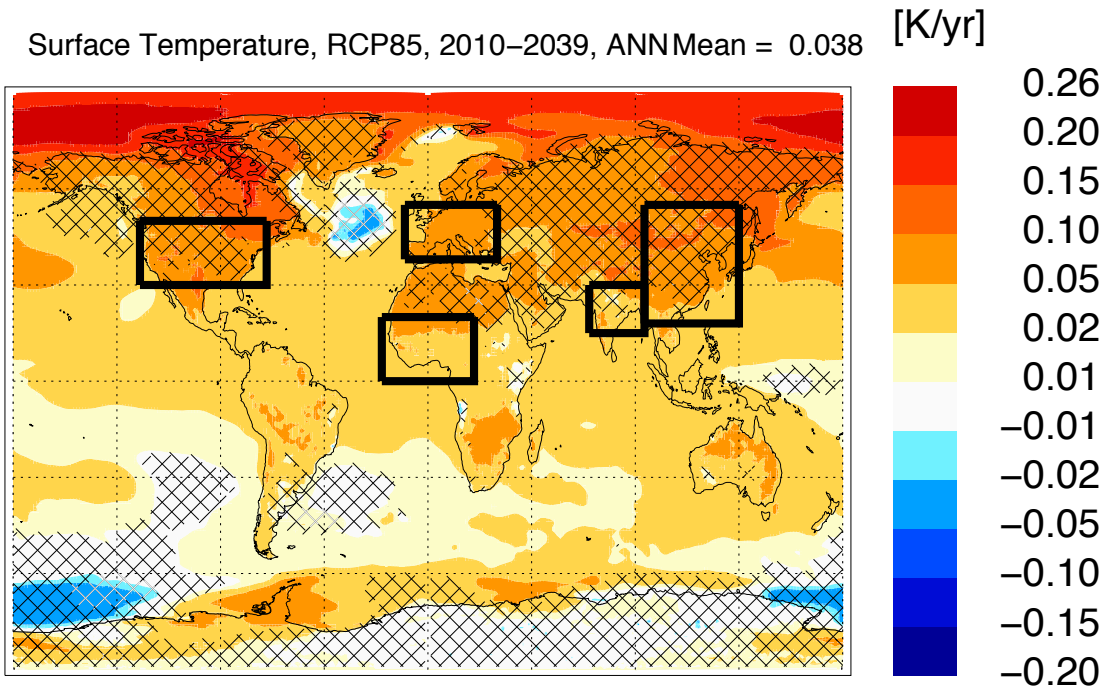

Figure 6S: Selected regions (black boxes) for regional averages, using land regions only: Northern America, Western Europe, West Africa, India, and China. Underlying colors show the surface temperature trends in K/year between 2010 and 2039 for RCP8.5. Hashed areas indicate a non-significant trend based on 25% significance level.

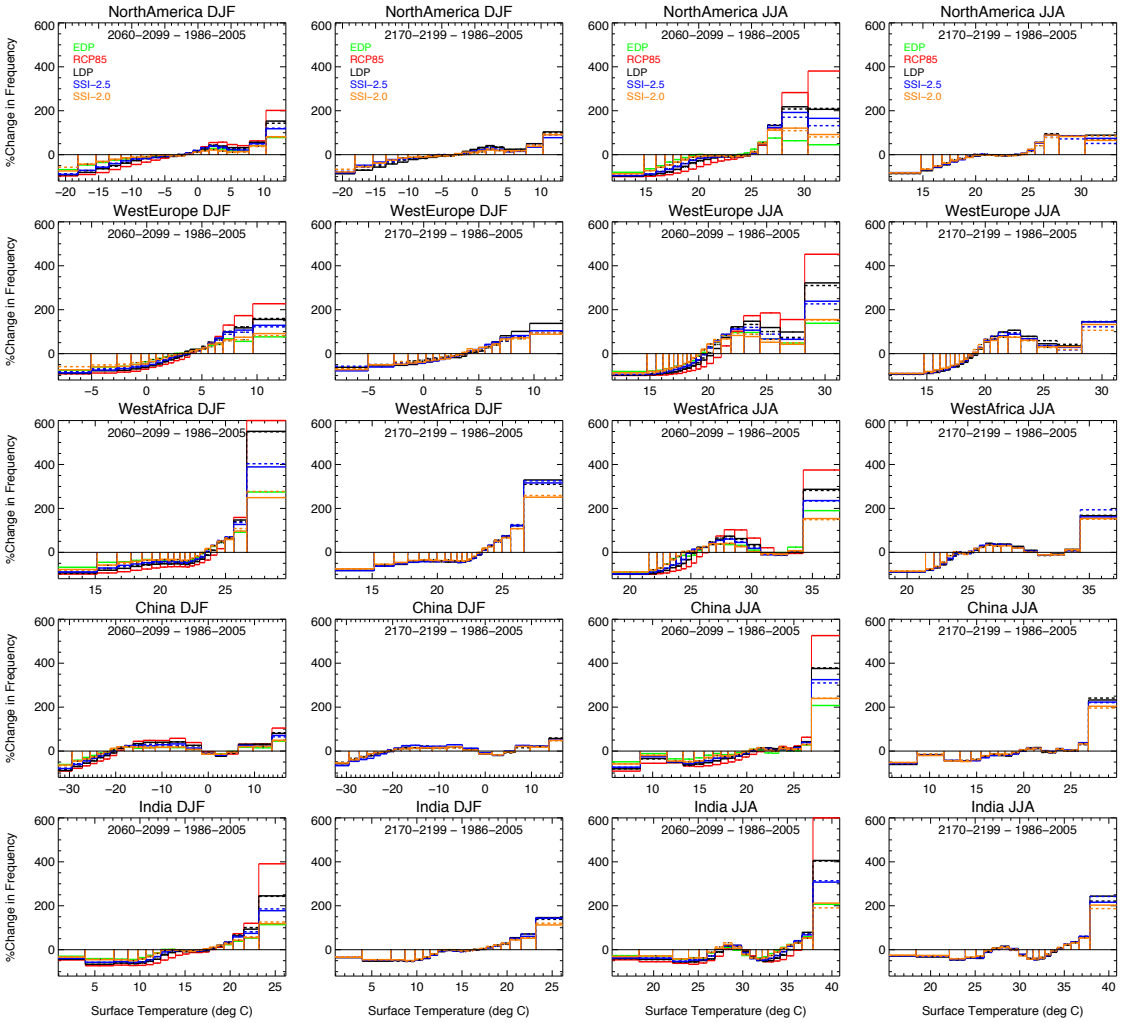

Figure 7S: Probability Density Function (PDF) of surface temperature changes compared to present day (1986-2005), for different experiments (colored lines) between 2060-2099 (first and third column) and between 2170-2199 (second and fourth column) and different seasons (December-January-February (DJF) on the left, and June-July-August (JJA) on the right) and all considered regions as defined in Figure S6 (shown in different rows). Second ensemble members of LDP, SSI-2.5 and SSI-2.0 is shown as a dashed line. Each bin of the PDF represents a fifth percentile of the distribution. The 95th percentile values for West Africa in DJF reach up to 700%.

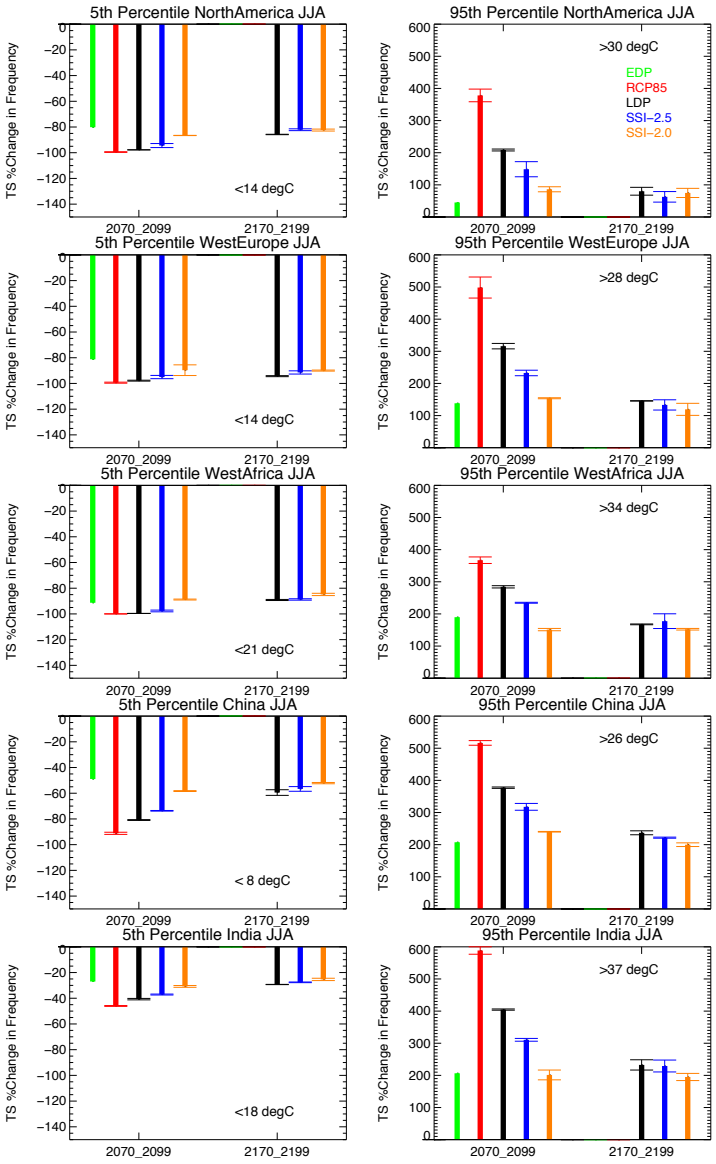

Figure 8S Relative change in the frequency of summer months, June-July-August (JJA), with extreme cold (left panels) and extreme heat (right panels), defined as monthly mean surface temperature below the 5th or above the 95th percentile of the probability distribution function for 2070-2099 and 2170-2199 compared to 1986-2005, for all considered, as defined in Figure S6. The value of the 5th and 95th percentile is illustrated in each panel. Error bars indicate the standard deviation of available ensemble members for each pathway.

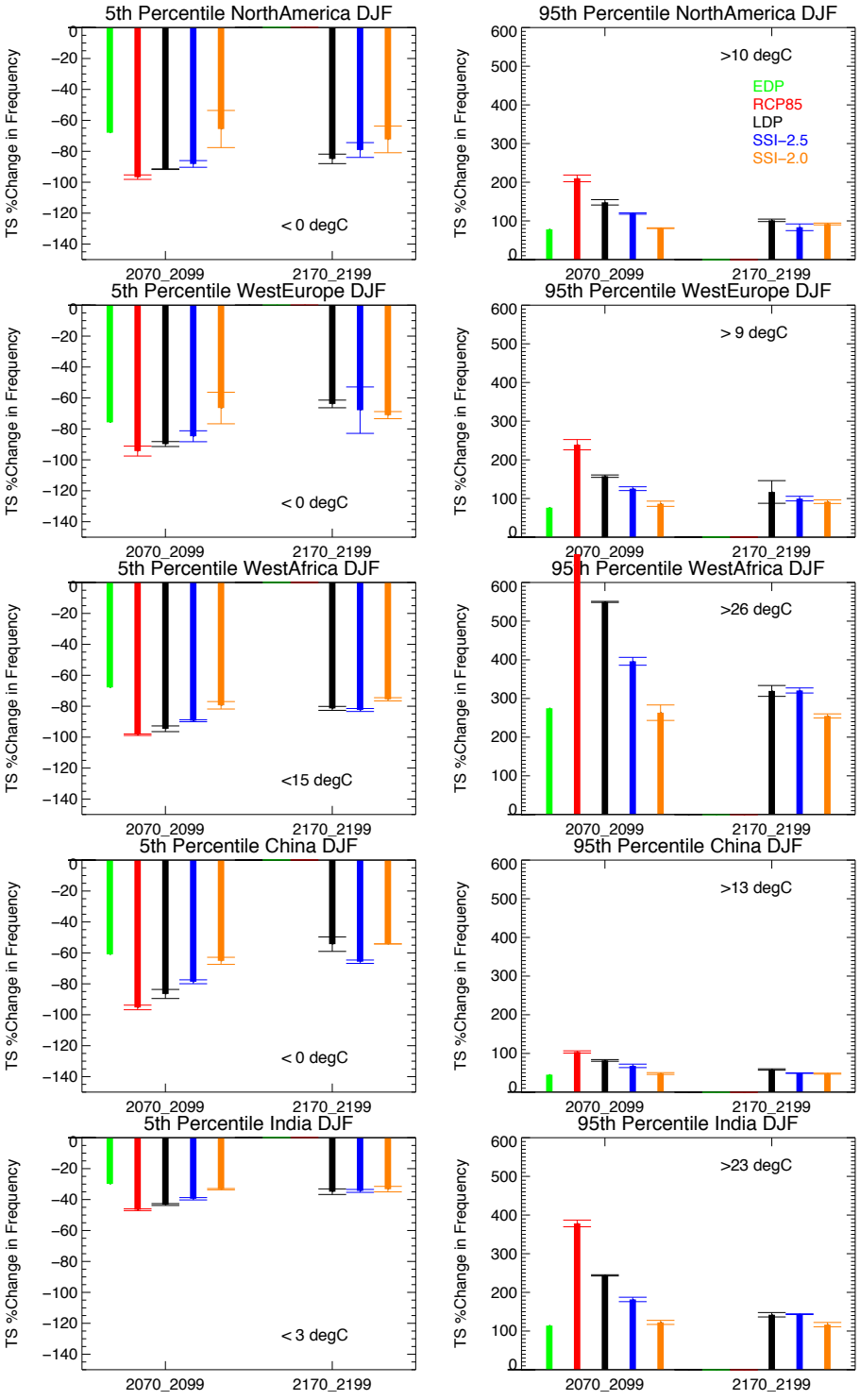

Figure 9S As Figure 7S, but for December-January-February (DJF) instead.

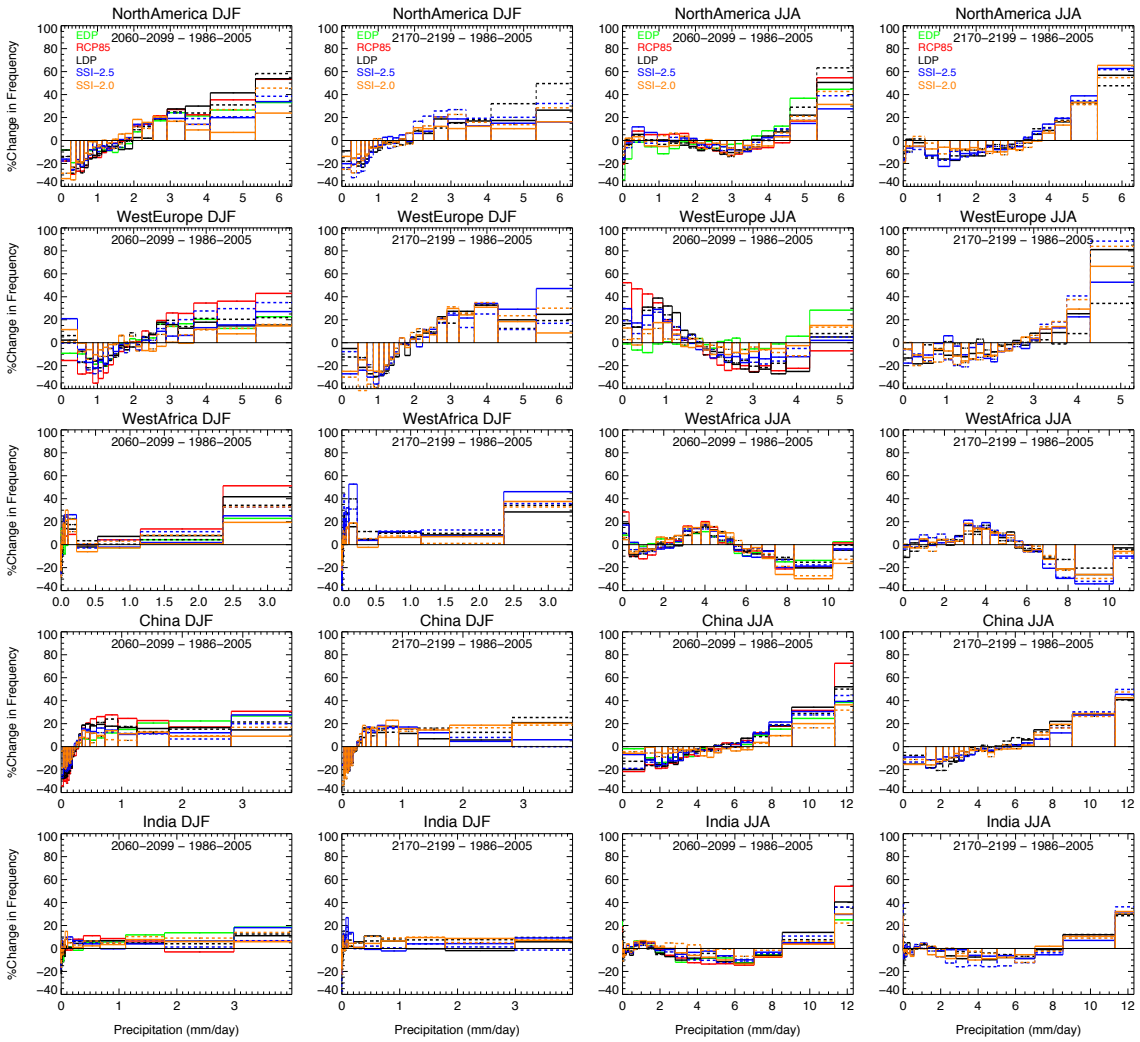

Figure S10: As Figure S6, but for precipitation instead.

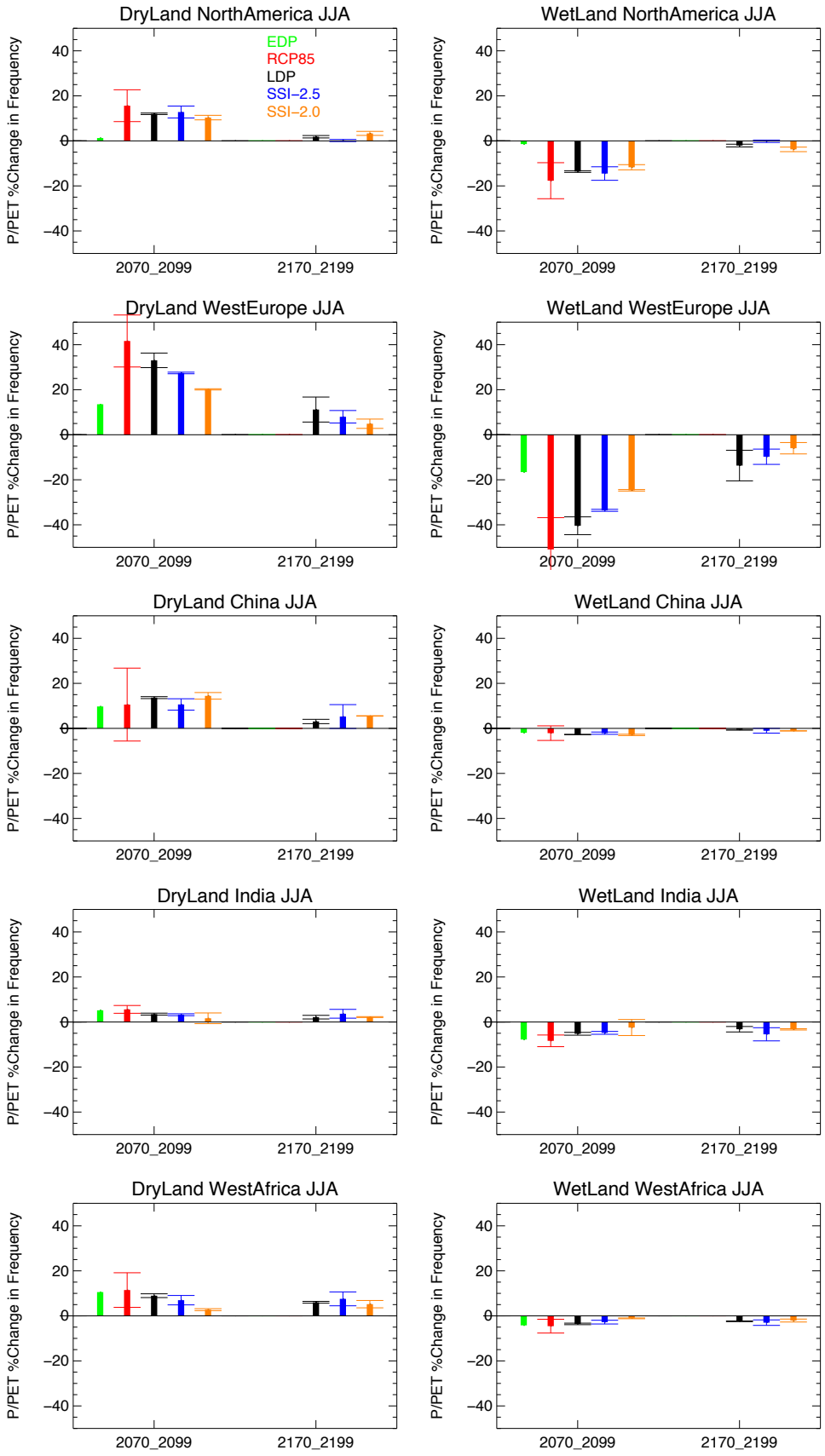
DryLand NorthAmerica JJA
WetLand NorthAmerica JJA
DryLand WestEurope JJA
WetLand WestEurope JJA
DryLand China JJA
WetLand China JJA
DryLand India JJA
WetLand India JJA
DryLand WestAfrica JJA
WetLand WestAfrica JJA
EDP
RCP85
LDP
SSI−2.5
SSI−2.0
P/PET %Change in Frequency
40
20
0
−20
−40
2070_2099
2170_2199

Figure S11: Relative change in the frequency of the aridity index (P/PET) for summer months over dry lands (left panels) and wet lands (right panels), defined as monthly mean aridity below or above 0.65 of the Aridity Index distribution for 2070-2099 and 2170-2199 compared to 1986-2005, for different all selected regions as defined in Figure S6. Error bars indicate the standard deviation of available ensemble members for each pathway.